



Numerical Study of Failure Mechanisms and Control Techniques for a Gob-Side Yield Pillar in the Sijiazhuang Coal Mine, China

Wen-da Wu^{1,2} · Jian-biao Bai^{2,3} · Xiang-yu Wang^{1,2} · Shuai Yan^{1,2} · Shao-xu Wu^{1,2}

Received: 20 December 2017 / Accepted: 8 November 2018 / Published online: 20 November 2018
© Springer-Verlag GmbH Austria, part of Springer Nature 2018

Abstract

Coal pillars are formed by excavation and mining activities in an intact coal seam and play a key role in underground coal mines. Most previous investigations of pillars have mainly focused on existing coal pillar failures. However, few scholars have investigated the failure mechanisms of coal pillars during their formation process. This paper focuses on the failure of a 7 m-wide coal pillar that caused the large deformation of a tailgate in the Sijiazhuang coal mine in China. Field tests and numerical modeling were used to study the initiation, propagation, and failure of cracks within this gob-side coal pillar during its formation. Field monitoring revealed that the maximum roof-to-floor and rib-to-rib convergence reached 860 mm and 1460 mm, respectively. The coal pillar became a yield pillar with substantial fractures. A numerical model was built using UDEC Trigon logic and calibrated with laboratory tests and RQD methods. Both the natural roadway deformation and crack distribution in the coal pillar were simulated. A FISH function was used to document the propagation of shear and tensile cracks in pillars with different W/H ratios, and a damage parameter was adopted to evaluate the failure of these pillars. The results suggest that the most appropriate pillar width is 10 m. Field trials prove that a 10 m-wide coal pillar combined with optimized support measures can effectively control deformation around the tailgate.

Keywords Yield pillar · Discrete element method · Failure mechanism · Crack propagation · Damage evolution · Support principle

1 Introduction

Coal pillars in underground coal mines play a key role in providing support to the superincumbent strata, isolating water and noxious gases from goafs, and maintaining the stability of the mining gateway (Salamon and Munro 1967). Gob-Side Entry (GSE) is an entry driven adjacent to an existing goaf with a 5- to 10-m yield pillar left in place to maintain the stability of roadway (Fig. 1b). GSE has been extensively employed in longwall mining in China (Bai et al. 2015; Li et al. 2015). By contrast, the majority of US and Australian longwall panels have four entries which are developed

and maintained on both sides of the panel, referred to as the Four-Entry System (Peng 2006; Carr et al. 1985). There are three rows of chain pillars designed into yield-stiff-yield configuration, where the yield pillars are designed to prevent coal bumps. However, the failure mechanisms of yield pillars are still not clear, and there are no straightforward and widely accepted yield pillar design criteria.

Generally, methods used to investigate the instability and failure of yield pillars can be divided into four types: the empirical method (Salamon 1970; Hill 2005), theoretical method (Poulsen 2010; Gao and Ge 2016), field measure method (Maleki 1992; Yu et al. 2016), and numerical simulation method (Wang et al. 2016a; Mortazavi et al. 2009). However, due to the heterogeneous and anisotropic nature of rock mass, the empirical formula and theoretical equation methods have large deviation. In addition, the field observation is time-consuming and costly. Numerical simulations can repeatedly calibrate the model parameters according to the field measurements for more reliable results. Hence, numerical simulations are a powerful tool for studying rock mechanics in underground excavation engineering. Many

✉ Jian-biao Bai
baijianbiao@cumt.edu.cn

¹ School of Mines, China University of Mining and Technology, Xuzhou 221116, China

² State Key Laboratory of Coal Resources and Mine Safety, Xuzhou 221116, China

³ Institute of Mining Engineering and Geology, Xinjiang Institute of Engineering, Urumqi 830091, China

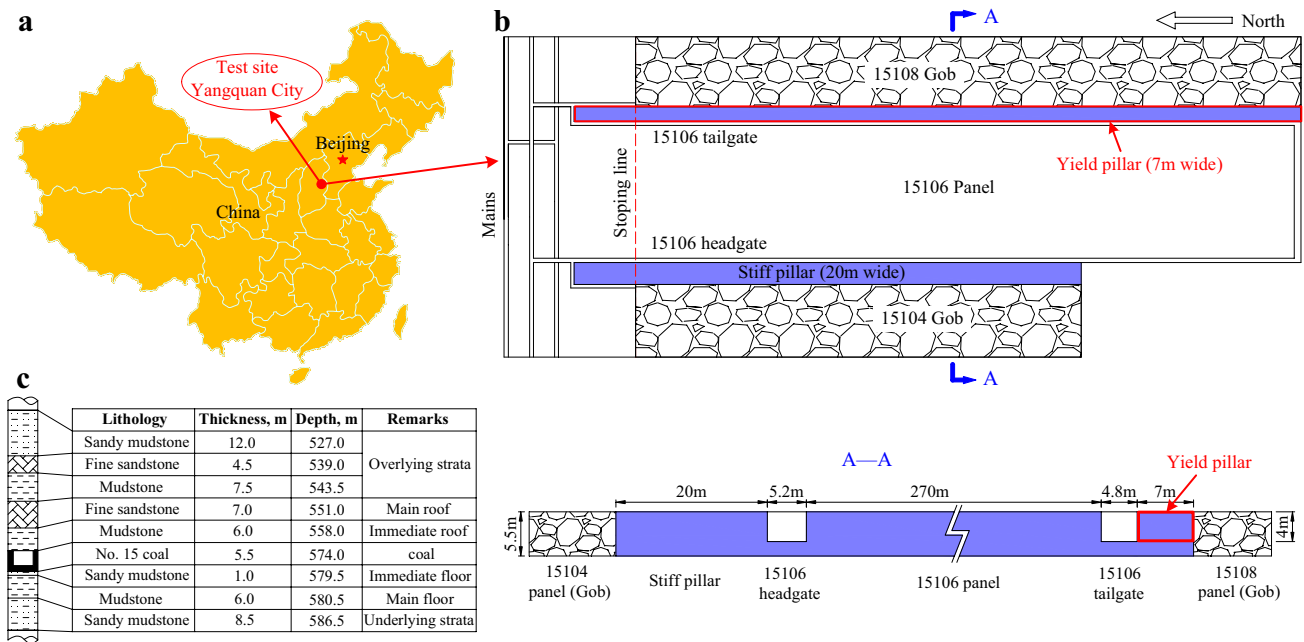


Fig. 1 Mine location and panel layout of the test site (**a** location of the test site, **b** panel, roadway layout and cross-section of study site, **c** generalized stratigraphic column of the test site)

scholars have developed numerical models using FLAC^{3D} code with strain-softening models incorporated to investigate the vertical stress and stability of yield pillars (Jaiswal and Shrivastva 2009; Zhang et al. 2017). But, standard strength-based strain-softening constitutive relationships cannot capture localization of failure as the lack of an internal length scale (De Borst 1993). Also, the continuum methods cannot explicitly simulated a fracture's generation development and propagation. One of the most popular explicit discrete element methods (DEM) is UDEC, which is widely applied to simulate the failure process of coal and rock mass (Lisjak and Grasselli 2014). In UDEC, a rock mass is depicted as a number of blocks delineated by joint sets. The joints between the intact rock blocks represent pre-existing discontinuities, and different constitutive criteria for joints and intact rock blocks are selected to simulate the significant deformations, rotations, and failures in rock mass (Itasca 2014; Gao 2013; Kazerani and Zhao 2010). Coulthard (1999) suggested that the UDEC model more closely approximates the real mechanics of the rock systems than a continuum model. Rock failure is captured either in terms of plastic yielding of the rock matrix or displacements of the discontinuities using the UDEC Voronoi model (Lorig and Cundall 1989). Furthermore, the UDEC Trigon model, as a non-continuous model based on Voronoi logic, overcomes many drawbacks inherent in traditional discrete element models (Gao and Stead 2014). Natural failure in the rock mass can be simulated because the cracks are generated in intact rock and propagated under different stress situations.

Therefore, the Trigon model can be employed to investigate the failure mechanisms of weak brittle materials and provide a more realistic representation of the rock micro-structure (Gao 2013).

Pine et al. (2006) introduced a new numerical modeling approach for naturally fractured rock masses. They embedded the data captured from rock face into a 3D model to fully account for pre-existing fractures. This approach makes it possible to study the tensile and compressive failure of rock masses along both pre-existing fractures and intact rock bridges (Elmo and Stead 2010). But, this approach can only capture fractures on exposed surface. Fractures within the solid are synthesized using FracMan code making them insufficiently accurate in many cases. It is generally known that coal pillars are formed by an intact coal seam through mining and excavation activities. However, the fractures on the exposed surface in underground engineering are also induced by mining and excavation, rather than naturally existing in the rock mass. Therefore, it is important to investigate the initiation and propagation of internal fractures as coal pillars are formed. Previous investigations have primarily studied cases of failed coal pillars.

This paper focuses on a 7 m-wide yield pillar in the tailgate of panel 15106 in the Sijiazhuang coal mine in China. A UDEC Trigon model is used to analyze the initiation, propagation, and failure of internal cracks from the micro-perspective during the formation of yield pillar. The model is validated by field monitoring. The damage in the yield pillar is documented and the failure

mechanisms explained. Finally, a technological solution is proposed to maintain the stability of yield pillar in the GSE.

2 Case Study

2.1 Description of the Mining and Geological Conditions

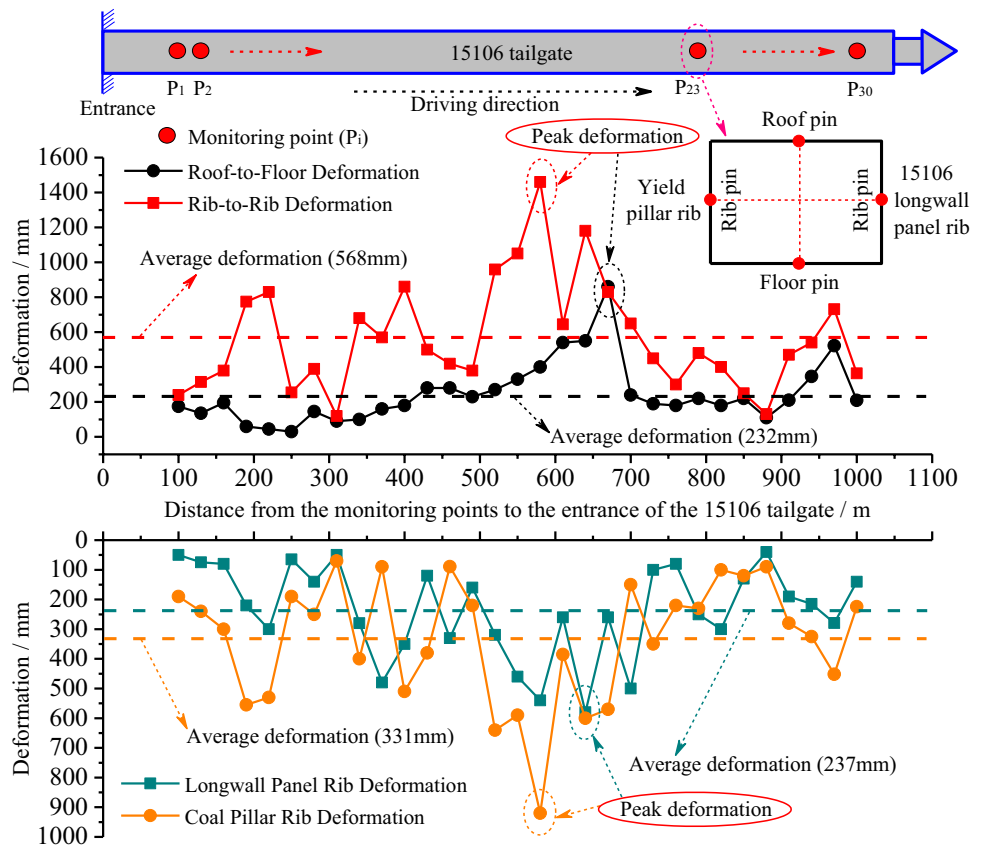
The Sijiazhuang coal mine is located in Yangquan, Shanxi province, China (Fig. 1a). Panel 15106 is in the #15 coal seam, and its average buried depth and thickness are 574 m and 5.5 m, respectively. The coal seam has numerous joints and fissures, 0°–12° dips, and a hardness of 1.5. The 15106 tailgate (4.8 m wide, 4.0 m high, and 1700 m long) is driven along the gob-side and roof of the coal seam. There is a 7 m-wide pillar between the 15106 tailgate and the 15108 gob. The layout of the roadway is shown in Fig. 1b. A generalized stratigraphic column for the mine is shown in Fig. 1c. The 15106 tailgate is seriously deformed as a result of the abutment stress imposed by the development of the 15108 gob side. The deformation is described below.

2.2 Roadway Deformation

Bolts were installed to support the roof and two ribs along the first 1000 m of the 15106 tailgate. Starting 100 m past the roadway entrance, monitoring stations were set up at 30 m intervals to monitor roadway deformation by cross section. Figure 2 shows the 15106 tailgate deformation between 100 m and 1000 m from the entrance. Roadway deformation is large and asymmetrical in the development period. The collected data on the GSE deformation can be summarized as follows: (1) the rib-to-rib convergence is larger than the roof-to-floor convergence. The maximum and average roof-to-floor convergences are 860 mm and 232 mm, respectively. The maximum and average rib-to-rib convergences are 1460 mm and 568 mm, respectively. The average rib-to-rib convergence is approximately 2.5 times that of roof-to-floor. (2) The yield pillar rib convergence is larger than the virgin coal rib convergence. The maximum yield pillar rib convergence reaches 920 mm, and the average convergence is 331 mm. By contrast, the maximum virgin coal rib convergence only reaches 580 mm, with an average convergence of 237 mm. The yield pillar rib convergence is approximately 1.4-times that of the virgin coal rib, indicating that it is very important to control the deformation of the yield pillar rib.

Figure 3 is a photograph of real scene in 15106 tailgate. It demonstrates that the yield pillar was fractured and

Fig. 2 Measured surrounding rock deformation in the 15106 tailgate



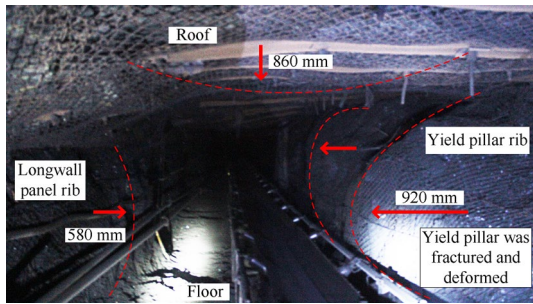


Fig. 3 Condition of the 15106 tailgate during the GSE

deformed. The large deformation is mainly caused by abutment stress, causing the yield pillar to become undersized. Therefore, yield pillar failure is very likely to affect the stability of GSE and should be studied to determine which pillar sizes and support methods can increase structural integrity.

2.3 Yield Pillar Damage

As illustrated in Fig. 4a, a horizontal exploratory borehole 4 m deep and 29 mm in diameter was drilled in the coal pillar rib 2 m above the floor. A YTJ20 borehole camera exploration device (BCED) was used to monitor the damage in yield pillar rib (Fig. 4b). Figure 4c shows probe images at different depths in the borehole. There are many inclined and intersecting cracks found around the borehole. The coal mass near the pillar rib has failed and become a fractured zone. In addition, based on the results of the borehole probe, it can be inferred that the deformation of the coal pillar adjacent to the gob side is larger or equal to that on the roadway side. Therefore, the entire coal pillar became fractured by the coalescence of internal cracks following the development of the 15106 tailgate.

3 Numerical Simulation Using Discrete Element Methods

3.1 UDEC Trigon Method

In the Trigon method, a rock mass is represented as an assembly of triangular blocks bonded through by inner contacts to simulate the brittle material (Gao 2013). Each triangular block is assumed to be elastic material and is divided it into triangular finite difference zones that cannot fail. Failure caused by shear or tensile stress can only occur along the contacts, depending on the strength of the contact surface. Mechanical interactions between two triangular blocks are controlled by Coulomb friction law as shown in Table 1.

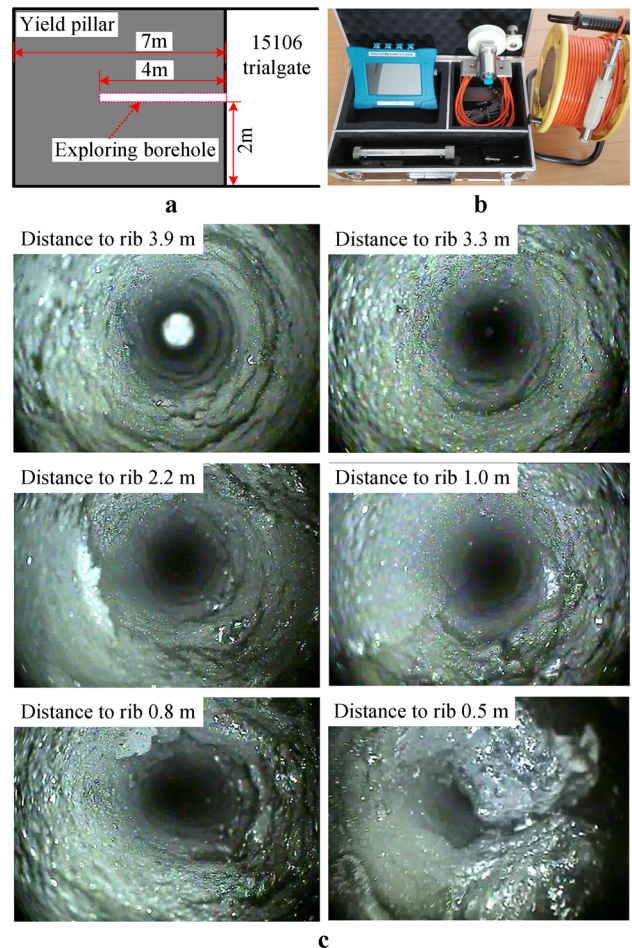


Fig. 4 Borehole camera exploration in the yield pillar. **a** Monitoring design. **b** Test equipment YTJ20-BCED. **c** Photographs obtained from borehole at different depths

Rock failure is captured by FISH language functions which monitor changes in micro-cracks.

3.2 Element Size and Homogenisation

In Trigon logic, the fracture process is developed from the microscopic elemental scale to the macroscopic scale. It is necessary to ensure that the pre-existing fractures are within the scale less than the triangular element size, so as to decouple the interaction of pre-existing and new fractures reasonably. Borehole mapping method was adopted to obtain statistics about pre-existing fractures length in the yield pillar and virgin coal seam, as depicted in Fig. 5. It demonstrates that both fracture length samples conform to a lognormal distribution. The dominant fractures length in pillar range from 0.03 to 0.19 m, accounting for 80% in total (Fig. 5a). In virgin coal seam, the fractures with length smaller than the 0.2 m account for 99.7% in total, and almost no large fractures (greater than 0.2 m) existing (Fig. 5b). Comparing the

Table 1 Failure criterion of the triangular blocks in the Trigon method

	<p>In the normal direction</p> $\Delta\sigma_n = -k_n\Delta u_n \tag{1}$ <p>Where $\Delta\sigma_n$ and Δu_n is the effective normal stress increment and normal displacement increment, respectively, and k_n is the normal stiffness of contacts. There is also a limiting tensile strength, σ_n^{\max}, is assumed for any contact. If this limit strength is exceeded, then $\sigma_n=0$.</p> <p>In the shear direction, if</p> $ \tau_s \leq c + \sigma_n \tan \varphi = \tau_s^{\max} \tag{2}$ <p>then</p> $\Delta\tau_s = -k_s\Delta u_s^e \tag{3}$ <p>or else, if</p> $ \tau_s \geq \tau_s^{\max} \tag{4}$ <p>then</p> $\tau_s = \text{sign}(\Delta u_s)\tau_s^{\max} \tag{5}$ <p>Where φ and c are the friction angle and cohesion of the contact, respectively. τ_s and σ_n are the shear and normal stress of the contact, respectively. Δu_n^e and Δu_s are the elastic component of the incremental shear displacement and total incremental shear displacement, respectively.</p>
<p>a Micro-contacts yielding process in Trigon model (Kazerani and Zhao 2010, Lisjak and Grasselli 2014)</p>	<p>b Coulomb friction law (Kazerani and Zhao 2010, Gao and Stead 2014)</p>

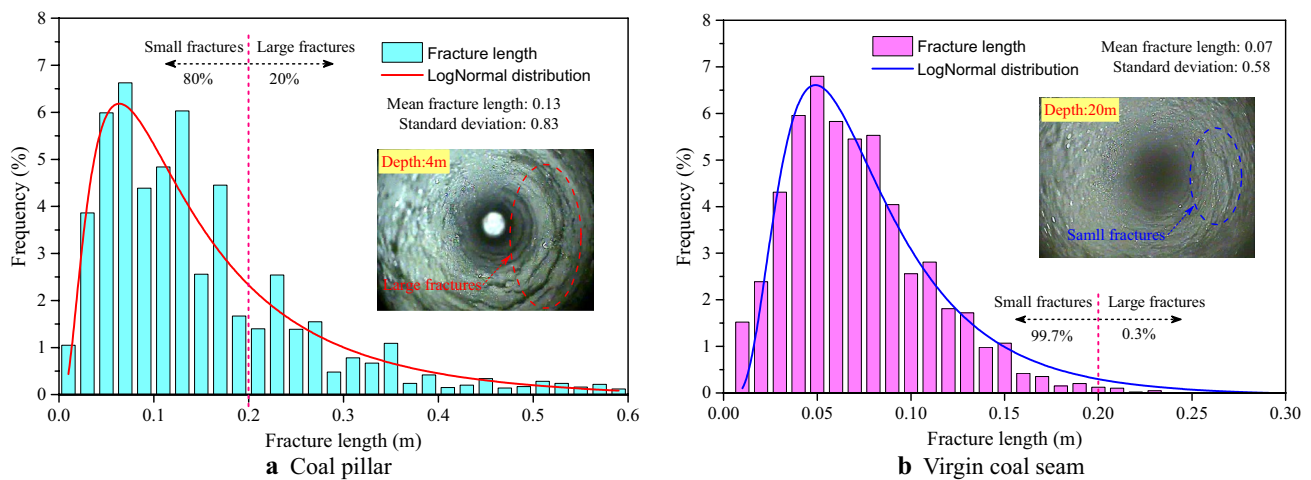


Fig. 5 Probability distribution of pre-existing fractures' length in the coal pillar (a) and virgin coal seam (b)

two figures, it was also found that the large fractures (20%) did not exist in virgin coal seam, but generated under mining activity, which cannot represent the natural pre-existing fractures. Thus, it is reasonable to choose 0.2 m as element size in the model to study the pillar width. Besides, the borehole images also show that the distribution of small pre-existing fractures is relatively uniform in the coal seam; therefore, the mesh should be as homogeneous as possible so that the fracture pattern is independent of the mesh in macro-scale fracture coalescence. The element generation typically does not take into consideration the influence of their homogenization (Mayer and Stead 2017).

3.3 Model Construction and Simulation Plans

A UDEC Trigon model was built to simulate the crack propagation process and the damage evolution of the yield pillar

during coal pillar formation. The size of the 2D model is 150 m wide \times 58 m high, as shown in Fig. 6a. For improving computational efficiency, UDEC Trigon logic was used to generate triangular blocks in the area of interest surrounding the roadway and pillar, as illustrated in Fig. 6b. The average edge length of these triangular blocks in the yield pillar area was 0.2 m, the surrounding coal area of the 15106 tailgate was 0.4 m, and the immediate roof and floor were 0.5 m. Areas surrounding the area of interest were assigned coarser rectangular blocks of progressively graded increasing edge length: 1.1 m, 2 m, and 7 m, respectively. These block sizes had been shown to be sufficiently fine to represent the mechanical behaviour of the coal pillar (Gao et al. 2015). The 80 m-wide panel 15108 was accounted for in the model to simulate the extraction of the adjacent coal panel and ensure realistic mining-induced stress on coal pillar (Fig. 6a). The bottom and lateral boundary were fixed

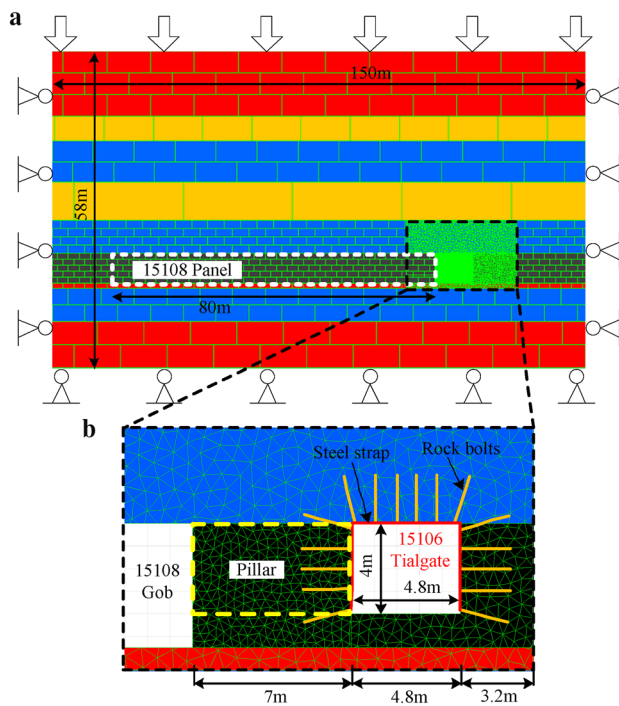


Fig. 6 Model overview. **a** Configuration of model using UDEC Trigon logic. **b** Dimensions of interest areas

in displacement at the vertical and horizontal direction, respectively. An in-situ stress state with $\sigma_v = 13.16$ MPa, $\sigma_H = 19.70$ MPa and $\sigma_h = 9.82$ MPa (Kang et al. 2009) was imposed in the model. The maximum and minimum horizontal stresses were perpendicular and parallel, respectively, to the direction of roadway development. The vertical stress of 13.16 MPa was applied on the up boundary to simulate overburden pressure.

In general, the simulation of the panel and roadway excavation comprised four steps. In first step, the geostatic stress condition was applied in the global model and solved. The 15108 panel was removed in the second step. Then the 15106 tailgate was developed in the third step. In the fourth step, seven different plans with different pillar W/H ratios (i.e., 1, 1.75, 2, 2.5, 3, 4, 5) were solved. Coal pillars with different W/H ratios are being used in various coal mines in the Yangquan coalfield. Hence, the simulation of these seven different yield pillars with various W/H ratios will be

helpful in developing yield pillar failure mechanisms and design criteria for roadway stability.

3.4 Calibration of the Simulation Parameters

The mechanical behaviour of the contacts is controlled by micro-properties including the normal and shear stiffness, tensile strength, cohesion, and frictional coefficient. It is often necessary to calibrate these micro-properties to the rock mass properties (Gao 2013; Kazerani and Zhao 2010). The following calibration process is applied to determine the rock mass micro-properties in the Trigon model (Gao and Stead 2014).

First, the rock mass's uniaxial compressive strength (UCS), deformation modulus, and Brazilian tensile strength (BTS) are determined from performing the laboratory unconfined compression test, Brazilian tests on small specimens, and field measurements (e.g. RQD, Q , GSI).

A calibration model was established using the Trigon logic. To eliminate the influence of block size on the outcome, the calibration model had the same triangular block size as the field-scaled model.

The deformation modulus should be calibrated by setting the blocks' deformation modulus equal to the rock mass's deformation modulus. The normal stiffness, K_n , is calculated according to Eq. (8). Poisson's ratio should then be calibrated by varying K_s/K_n . The ratio of K_s/K_n is set to 0.2 in this work.

Using the calibration model to run a series of unconfined compression tests and Brazilian tests. The strength properties assigned to the contacts must be adjusted until the UCS, deformation modulus, and BTS are agreement with the rock mass properties. This involves three sub-steps: first, the contact chesion, then the friction angle, followed by the tensile strength.

3.4.1 Rock Mass Properties

The intact parameters obtained by performing compression tests and Brazilian tests on small specimens are listed in Table 2. But, these parameters cannot predict the natural deformability of rock mass. RQD is still widely applied to estimate the rock mass deformation modulus because it is often more easily acquired than RMR or Q (Hoek and

Table 2 Properties of intact rock and calculated rock mass in the Sijiazhuang coal mine

Rock strata	Intact rock		RQD	Rock mass		
	E_r (GPa)	σ_c (MPa)		E_m (GPa)	σ_{cm} (MPa)	σ_{tm} (MPa)
Fine sandstone	23.4	48.9	92	14.8	36.6	3.66
Mudstone	10.6	16.6	76	3.4	8.1	0.81
Coal	3.2	10.5	72	0.86	4.6	0.46
Sandy mudstone	14.2	21.0	85	6.6	13.0	1.30

Brown 1997). Based on much field monitoring data, Zhang and Einstein (2004) developed a relation, Eq. (6), between RQD and the modulus ratio E_m/E_r , where E_m and E_r are the deformation modulus of the rock mass and the intact rock, respectively. Hence, this recommended relation can be used to calibrate the rock mass parameters. The RQD value of the rock mass was observed using a borehole camera in our studied site.

$$E_m/E_r = 10^{0.0186RQD-1.91} \tag{6}$$

The rock mass strength can be calculated by Eq. (7) (Singh and Seshagiri 2005):

$$\left(\frac{\sigma_{cm}}{\sigma_c}\right) = \left(\frac{E_m}{E_r}\right)^n \tag{7}$$

where σ_{cm} and σ_c are the UCS of rock mass and intact rock, respectively. And the index n for splitting, shearing, sliding and rotation modes are 0.56, 0.56, 0.66, and 0.72, respectively. Since the failure process of coal pillars is very complicated, there are many failure models. For the purposes of this paper, the value of index n is 0.63.

The properties of the intact rock and calculated rock mass are listed in Table 2. The tensile strength of the coal and rock mass was estimated to be one-tenth of the compressive strength (Gao et al. 2015).

3.4.2 Contact Micro-Parameters

The above procedure was followed to calibrate the contact micro-parameters of different strata layers in the Trigon model. The Trigon logic calibration models were established for simulating the UCS and BTS with dimensions of 2 m-wide \times 4 m-high and 2 m-diameter, as illustrated

in Fig. 7. Since the models are composed of four kinds of lithology, four contact types must be calibrated. The normal and shear stiffness of contacts, K_n and K_s , were calculated using the Eq. (8), where K and G are bulk and shear modulus of the blocks, respectively; ΔZ_{min} is the smallest width of the zone adjoining the contact in the normal direction, and n is a multiplication factor (usually set to 10). K and G were calculated using $K = E/3(1 - 2\mu)$ and $G = E/2(1 + \mu)$, where μ is Poisson's ratio of blocks (Itasca 2014).

$$K_n = n \left[\frac{K + (4/3)G}{\Delta Z_{min}} \right] \quad 1 \leq n \leq 10. \tag{8}$$

The input parameters of the blocks and contacts were calibrated using an iterative, trial-and-error method to match the rock mass properties given in Table 2. The calibrated micro-properties in the Trigon model are provided in Table 3. These properties represent the rock mass properties at the studied site. The calibration results are listed in Table 4.

The joint model residual version of the Coulomb model used in the simulation assumes that the failed contacts have zero cohesion, tensile strength and residual friction angle.

3.4.3 Rock Bolt and Cable Properties

After the 15106 tailgate was developed, the roof and two ribs were supported by resin-anchored rock bolts 22 mm in diameter and 2.2 m in length. The spacing of bolts in the roof and two ribs is 880 mm and 900 mm, respectively. The roof bolts were installed with W-shaped steel straps, and rib bolts were installed with steal ladder beams. In the model, the steel straps and steal ladder beams were represented as built-in "Liner" elements and the rock bolts were represented as a

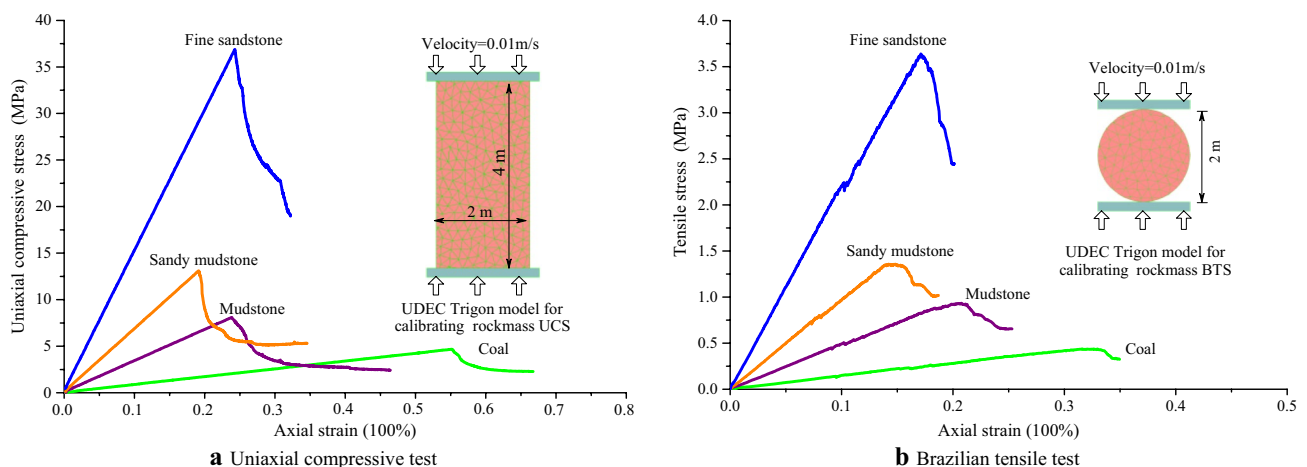


Fig. 7 Calibration model using Trigon logic for calibrating the rockmass properties shown in Table 2. a Uniaxial compressive test, b Brazilian tensile test

Table 3 Calibrated micro-properties in the Trigon model for field scale model

Rock strata	Matrix properties			Contact properties				
	Density (kg/m ³)	<i>E</i> (GPa)	Poisson's ratio	<i>k_n</i> (GPa/m)	<i>k_s</i> (GPa/m)	Cohesion (MPa)	Friction angle (°) (peak/residual)	Tensile strength (MPa)
Fine sandstone	2600	14.8	0.28	757	151	11.7	40/33	5.55
Mudstone	2100	3.4	0.26	166.4	33.3	2.7	36/30	1.23
Coal	1300	0.86	0.25	160	32	1.5	35/30	0.41
Sandy mudstone	2350	6.6	0.28	337	67.5	4.2	38/32	1.97

Table 4 Calibrated results of rock mass properties in the Trigon model

Rock strata	<i>E</i> (GPa)		Error (100%)	UCS (MPa)		Error (100%)	BTS (MPa)		Error (100%)
	Target	Calibrated		Target	Calibrated		Target	Calibrated	
Fine sandstone	14.8	15.07	1.82	36.6	36.87	0.74	3.66	3.65	- 0.27
Mudstone	3.4	3.37	- 0.88	8.1	8.12	0.25	0.81	0.89	9.88
Coal	0.86	0.84	- 2.33	4.6	4.67	1.52	0.46	0.44	- 4.35
Sandy mudstone	6.6	6.74	2.12	13.0	13.14	1.08	1.30	1.36	4.62

Table 5 Properties of support elements in Trigon model as proposed by Gao and Stead (2015)

Type	Value
Cable element	
Elastic modulus (GPa)	200
Stiffness of the grout (N/m ²)	2e9
Cohesive capacity of the grout (N/m)	4e5
Structural element	
Elastic modulus (GPa)	200
Tensile yield strength (MPa)	500
Compressive yield strength (MPa)	500
Interface normal stiffness (GPa/m)	10
Interface shear stiffness (GPa/m)	10

built-in “Cable” elements. The support elements properties used in this study are listed in Table 5.

3.5 Validation of the Global Model

3.5.1 Simulated Roadway Deformation Comparison with Field Observations

The deformation of the 15106 tailgate was modeled by the numerical simulation using the same rock properties and excavation techniques used in the Sijiazhuang coal mine. Figure 8 shows a comparison between the result of the numerical simulation and the monitoring. The roof-to-floor and rib-to-rib convergence, as calculated by the numerical model, are approximately 592 mm and 696 mm, respectively.

This is nearly the same as the roadway deformation recorded by the field monitoring station located 610 m from the roadway entrance (Fig. 8a). Actual convergence at that location was 540 mm from roof-to-floor and 645 mm from rib-to-rib (Fig. 8b). Figure 8c–g compares photographs of the actual roadway damage with the simulated deformation of the roof and rib in roadway cross-sections. The deformation of the floor rails occurred because of floor heave, which also broke the steel strap in the roof. The roof subsidence and rib bulge were caused by mining-induced stress acting on the roadway. The greatest deformation occurred in the lower half of the coal pillar, and the transportation belts became extruded. All roadway damage that was monitored in the field was reproduced by the UDEC Trigon model, as shown in Fig. 8f.

3.5.2 Simulated Fractures and Borehole Camera Image Comparison

The distribution of cracks in the 7 m-yield pillar were obtained from the Trigon model, as shown in Fig. 9. The model shows that the coal pillar can be divided into a large fractured zone (LFZ) and a small fractured zone (SFZ), according to the number of cracks. Figure 9b shows that the LFZ, mainly consisting of tensile cracks, was formed in both sides of the yield pillar. While, the SFZ mainly consisting of shear cracks, was generated in the center of the yield pillar. These simulation results are in agreement with the borehole images shown in Fig. 4c.

The model results are close agreement with the field observations, verifying that the model can be used to simulate the deformation and failure of coal pillars and roadways.

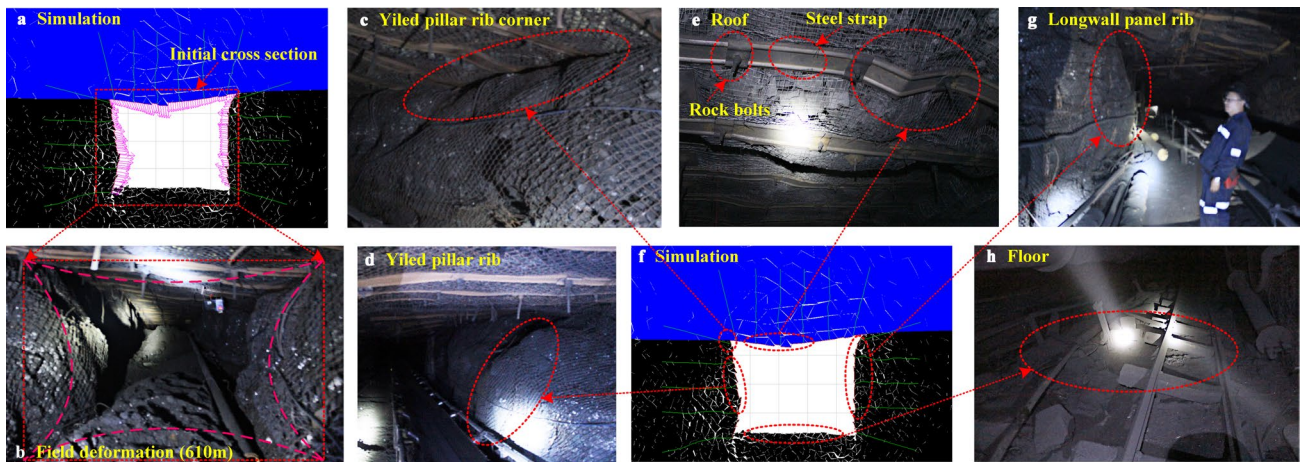


Fig. 8 Comparison of the simulation results and field observations

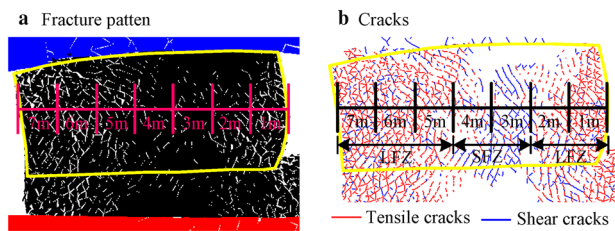


Fig. 9 Trigon model predicted fractures distribution in the pillar. a Fracture pattern, b cracks distribution

The following sections will analyze crack propagation and damage of coal pillars with different widths in a GSE and investigate the failure mechanisms using this UDEC Trigon model.

4 Modeling Results

4.1 Damage Analysis

To monitor the failure of the coal pillar during its formation process, a FISH function was used to record the total length of cracks in the pillar as well as the length of shear and tensile cracks caused by mining-induced stress. The damage parameter, D , is proposed according to Gao (2013):

$$D = \frac{L_S + L_T}{L_C} \times 100\%, \tag{9}$$

where L_C is the total contact length, L_S is the total length of shear cracks, and L_T is the total length of tensile cracks. The damaged region indicates that contacts have failed in different degrees due to either shear or tensile stress.

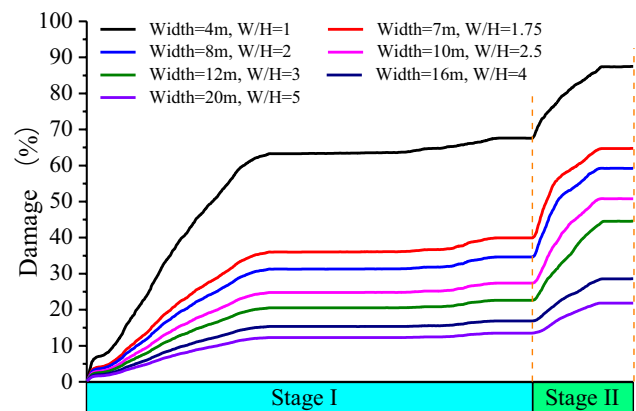


Fig. 10 Damage evolution process in pillars with different W/H ratios in Stage I and Stage II

Figure 10 shows how the damage parameter changes in coal pillars of different widths, including during 15108 longwall mining (Stage I) and 15106 tailgate excavation (Stage II).

Stage I: The coal mass was damaged by 15108 longwall mining. The larger distance from the gob side, the less damaged the coal mass will be. The damage parameter, D , for coal in the coal pillars with widths of 4, 7, 8, 10, 12, 16, and 20 m were 67.6%, 39.9%, 34.6%, 27.4%, 22.6%, 16.9%, and 13.5%, respectively.

Stage II: The damage parameters for the different widths of coal pillars increased greatly during the development process of the 15106 tailgate. The increase of damage parameter can be divided into three stages: a stage of sharp increase, a stage of linear increase, and a stable stage. The damage parameter, D , for coal pillars with widths of 4, 7, 8, 10, 12, 16, and 20 m were 87.5%, 64.8%, 59.2%, 50.8%, 44.6%, 28.3%, and 21.8%, respectively. As such,

the greater the width of the coal pillar, the less significant the damage.

4.2 Crack Analysis

This section analyzes the propagation of cracks in coal pillars of different widths during the formation process, as shown in Fig. 11.

Stage I: The cracks in the coal pillar propagate continuously as the rock above the gob caves. Figure 11a, b shows that the shear and tensile cracks are almost the same quantities in coal pillars with different W/H ratios before the 15106 tailgate is excavated, indicating that the most fracturing takes place within the 4 m of the coal pillar near the gob side.

Stage II: Cracks continue to propagate as the 15106 tailgate starts to be excavated, finally stopping after the excavation is completed (Fig. 11a, b). Evidently, the amount of shear cracks in the pillar is greater than that of tensile cracks, which implies that pillar damage is caused mainly by shear failure.

4.3 Failure Mechanism

After the coal pillar is formed, the damage parameters at different positions of different widths pillars are shown in Fig. 12. The damage mainly occurs in both the roadway and gob sides of the coal pillar and appears in a “U”-shaped distribution. Gao (2013) proposed $D = 35\%$ as a critical value for classifying failure areas and used it to analyze roof collapse above a longwall panel. This percentage is, therefore, adopted to evaluate the degree of damage in the pillars of our study. When $W/H \leq 2$, the entire coal pillar is fractured and it is deemed a high damage area (HDA) ($D > 35\%$). When $W/H \geq 2.5$, a low-damage area (LDA) ($D < 35\%$) is located at the center of the coal pillar. This LDA expands as the W/H ratio increases.

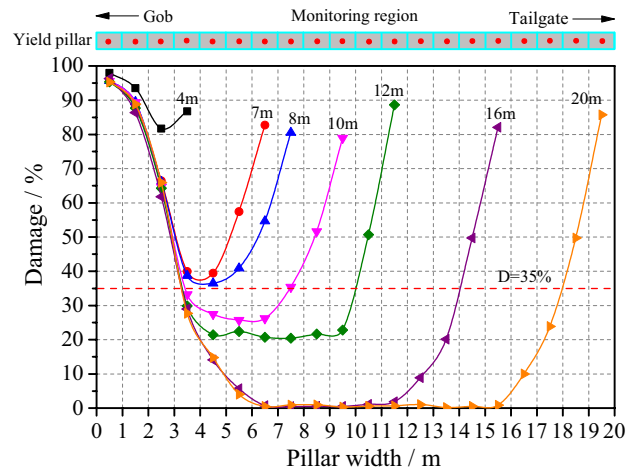


Fig. 12 Distribution of the damage parameter, D , in pillars of different widths

The fracture patterns and crack distributions in coal pillars with different widths are shown in Fig. 13. When the width of the coal pillar is 4 m (Fig. 13a), the coal pillar is completely fractured, mainly as a result of tensile failure. When the width is 7 m or 8 m (Fig. 13b, c), the HDA encompasses the entire coal pillar and the internal joints become sheared from sliding. Tensile failure mainly occurs near the coal pillar boundary and shear failure mainly occurs at the center of the pillar. When the pillar width increases from 10 to 20 m (Fig. 13d–g), the HDA appears as “U” shaped, and the widths of gob-side and roadway side HDA are 4 m and 2 m, respectively. On the other hand, the LDA appears in an “X” pattern within the pillar, and the width of the LDA changes from 4 to 14 m. The stability of the coal pillar improves when the range of the LDA increases.

To summarize, the failure mechanism of the coal pillar is as follows: the internal joints are initially sheared by

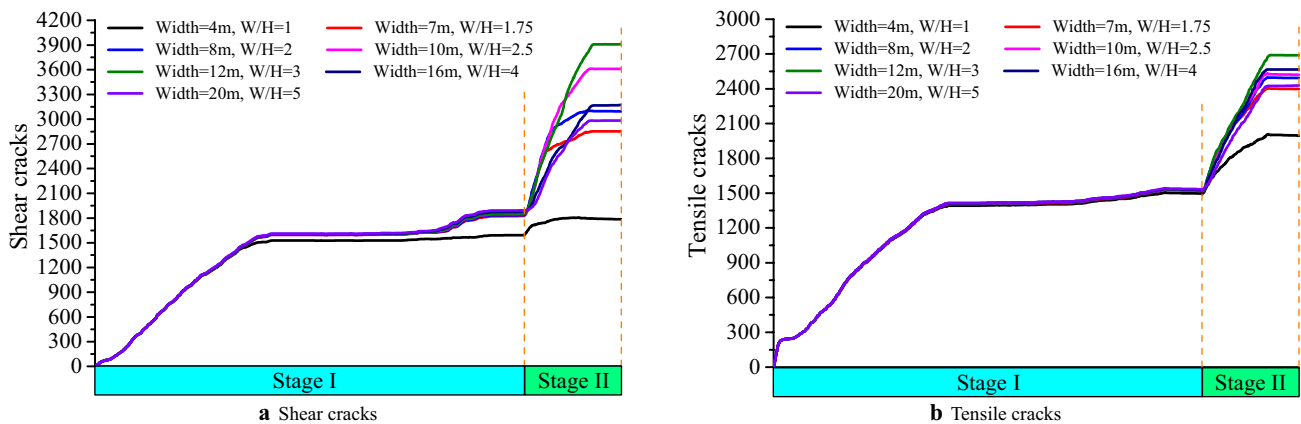


Fig. 11 Cracks in the pillar with different W/H ratios in Stage I and Stage II. a Shear cracks, b tensile cracks

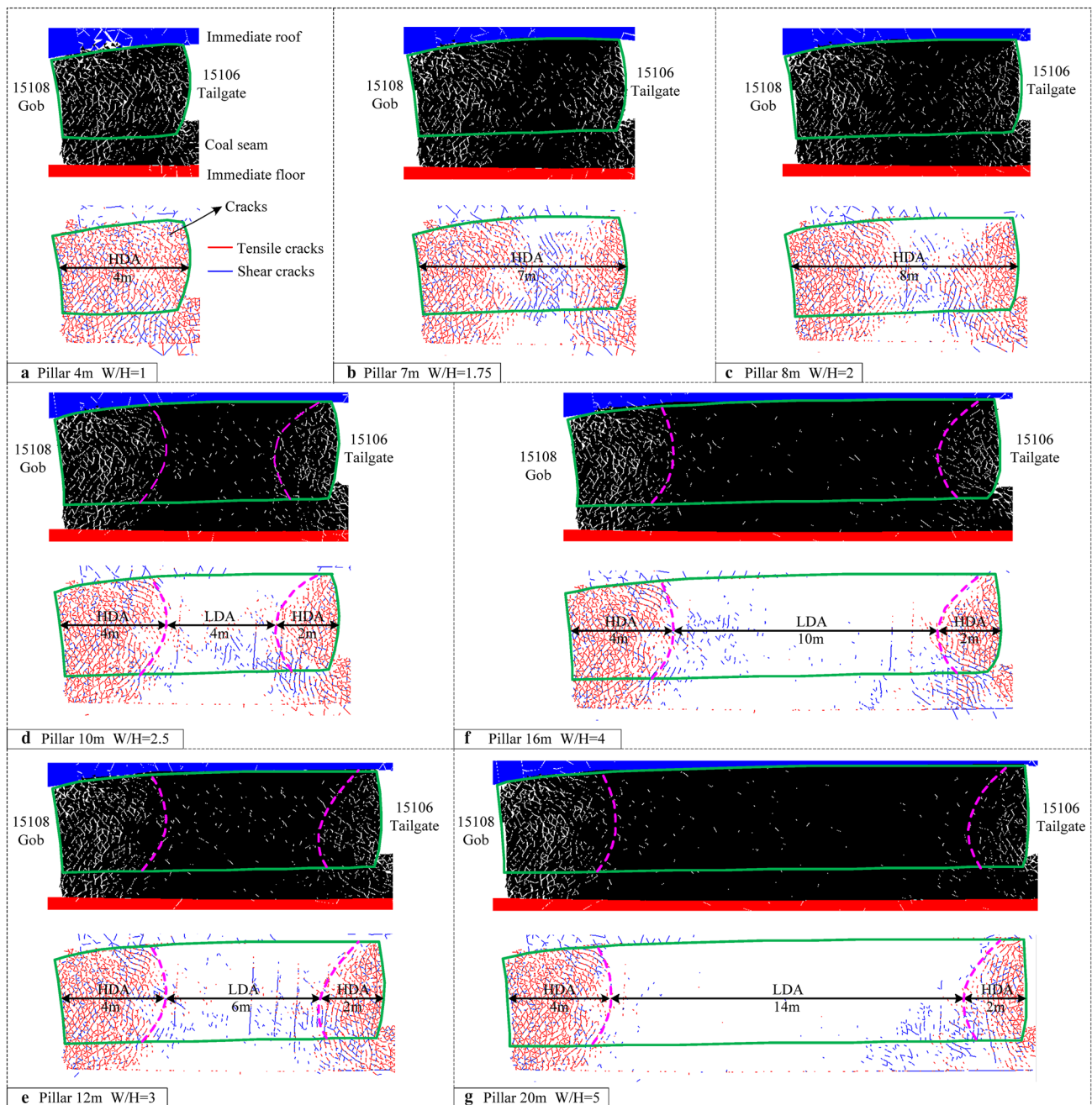


Fig. 13 Fracture patterns and micro-tensile and micro-shear fractures in pillars of different widths. The red cracks represent tensile cracks, blue cracks represent shear cracks, green solid lines represent

the boundary of the coal pillar, magenta dashed lines represent the boundary of the HDA, and the arrows show the width of the damaged area

mining-induced stress. Then, tensile failure occurs under constant pressure. Importantly, obvious macro-cracks appear as a result of coal splitting in the HDA. Failure spreads from the edge to the center of the coal pillar, and the failure degree decreases as it spreads. Therefore, it is essential to choose the best possible coal pillar width and to focus on controlling the area where macro-cracks appear to keep the pillar from collapsing.

5 Discussion

5.1 Yield Pillar Width Determination

The results from the BCED and numerical simulations show that the width of the coal pillar and applied support measures could not sufficiently control the roadway deformation. Comparing the Sijiazhuang coal pillar to other intact

Chinese coal mines (Wang et al. 2016b) reveals that the most significant deformation of the roadway was likely caused by damage to the 2 m of superficial rock surrounding the roadway. Uneven deformation occurred due to shear slip of fractured coal pillar. An appropriate pillar size would reduce deformation and maintain stability of the yield pillar. Figure 14 shows the damage parameter at a depth of 2 m in coal pillar ribs with different W/H ratios. When the width of the coal pillar is 10 m, the damage parameter is low and roadway deformation can be easily controlled. Thus, we conclude that the LDA is at the center of coal pillar when $W/H \geq 2.5$, and that a 10-m coal pillar would have good bearing capacity. According to our analysis, a secure coal pillar width is 10 m.

5.2 Support Principles

Based on the failure characteristics of yield pillars, the following support measures are proposed: (1) high-strength elongated bolts should be used in combination with anchor cables to control shallow fractured zones and prevent bed separation from the surrounding rocks, (2) high-pretension bolts should be applied in yield pillar ribs to control

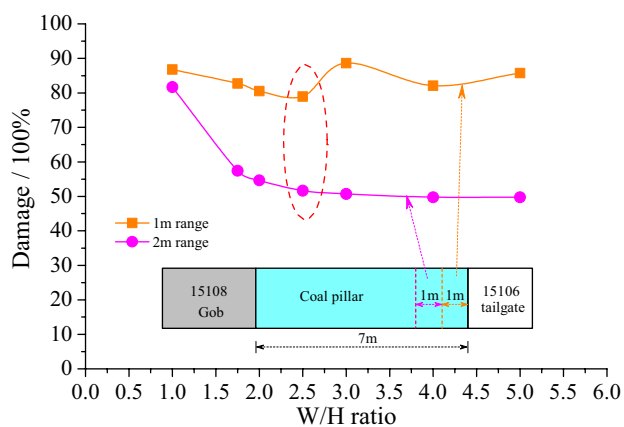


Fig. 14 Damage parameter at a depth of 2 m in coal pillar ribs with different W/H ratios

uneven deformation caused by shear slip on the joints in shallow fractured zones. High-power pneumatic wrenches (Fig. 15a), torque amplifiers (Fig. 15b), and torque wrenches (Fig. 15c) can increase the pretension force on bolts, (3) the parts selected for rock bolts and anchor cables should significantly contribute to controlling surface fracturing and preventing cracks propagation in the yield pillar. The W-shaped steel strap plates for bolts (Fig. 15d) and high-strength dish-shaped steel plates for anchor cables (Fig. 15e) should be adopted and used in conjunction with steel ladder beams (Fig. 15f), (4) grouting reinforcement should be used to improve the residual strength of shallow fracture zones in yield pillar ribs.

5.3 Technical Measures

In accordance with the above description, the yield pillar width was increased to 10 m and optimized support measures were adopted in the last 600 m of 15106 tailgate. A cross-section of the optimal support pattern is illustrated in Fig. 16.

The roof was supported by high-strength left-hand-threaded steel bolts 22 mm in diameter and 2200 mm in length. The inter-row spacing of the bolts was 880 mm × 800 mm. Nineteen-strand steel anchor cables 21.8 mm in diameter and 7200 mm in length were also used for roof support. The inter-row spacing for the cables was 1800 mm × 1600 mm (2 cables per row) and 1200 mm × 1600 mm (3 cables per row). The two ribs were supported by high-strength left-hand-threaded steel bolts 20 mm in diameter and 2200 mm in length. The inter-row spacing of the bolts was 900 mm × 800 mm. Seven-strand steel anchor cables 17.8 mm in diameter and 4200 mm in length were used in the longwall panel rib. The inter-row spacing of these anchor cables was 1800 mm × 1600 mm. The bolts and anchor cables were connected with steel ladder beams made of 12 mm round steel (Figs. 15f, 16b). Bolts in the roof and rib corners were installed at a 15° incline. In addition, all bolts and

Fig. 15 Photograph of installation equipments and rock bolt components. **a** High-power pneumatic wrench. **b** Torque amplifier. **c** Torque wrench for rock bolts. **d** Bolt plate of W-shaped steel straps. **e** Cable plate of high-strength dish-shaped steel. **f** Steel ladder beam

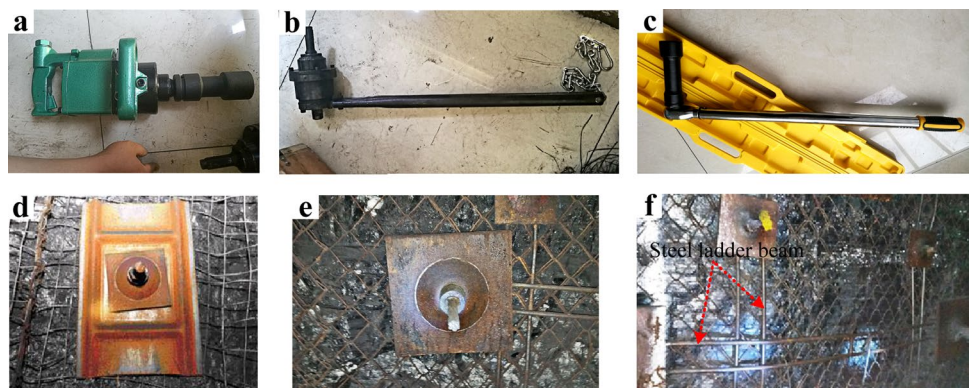


Fig. 16 Detailed technical parameters in 15106 tailgate. **a** Entry section supported by bolt and anchor cable. **b** Support pattern in yield pillar rib

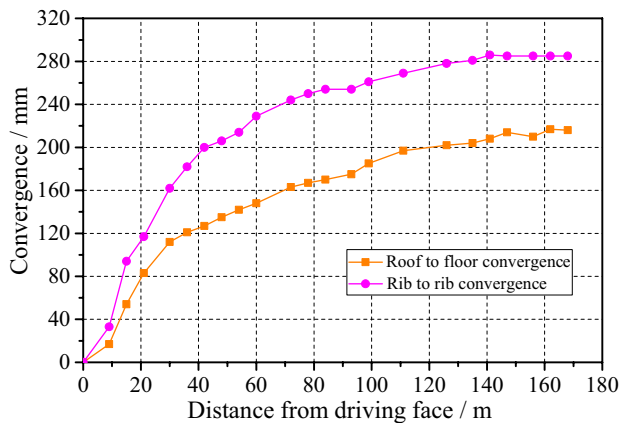
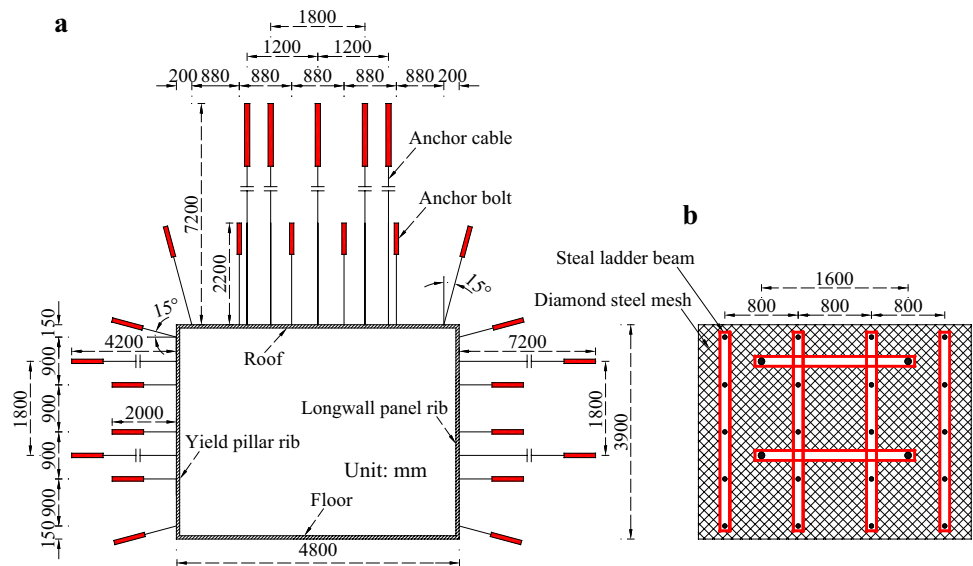


Fig. 17 Measured convergences in the 15106 tailgate using optimal support measures and pillar width

anchor cables in the roof and two ribs were installed with pretension forces of 50 kN and 250 kN, respectively.

The deformation during the driving process of the 15106 tailgate with the above optimized support measures are shown in Fig. 17. Monitoring results show that deformation of rocks surrounding the tailgate is effectively controlled, and the tailgate stabilizes after driving 140 m. The roof-to-floor and rib-to-rib convergences were 216 mm and 285 mm, respectively, representing a reduction of 78.9% and 80.5% compared to convergences prior to the implementation of these support measures. The results demonstrate that a 10-m pillar with optimal support measures can successfully control the deformation of surrounding rock.

5.4 Further Research

A Trigon model is used to study the failure process of gob-side coal pillar. There are no pre-existing large fractures (greater than 0.2 m) in coal seam according to the borehole mapping methods, and these large fractures were not explicitly represented in the model. Meanwhile, the Trigon method controls the homogeneity of blocks by iteration times, and the generated element typically does not take into consideration the heterogeneity influence. Although this method has certain limitations at field scale, e.g. overestimates the pillar strength (Gao and Kang 2016) or changes the failure mechanism of the pillar (Mayer and Stead 2017), the application presented has relevant information for those working in these themes. As a result, the outlined limitations should not preclude the method or results; however, caution needs to be taken when analyzing the pillar strength and failure mechanism, as additional research is required to further analyse the pre-existing large fractures and the heterogeneities based on the synthetic rock masses (SRM) method (Pine et.al 2006; Elmo 2006).

6 Conclusions

A field test and numerical simulation were combined to investigate the micro-cracks' propagation and failure law of coal pillar in the Gob-Side Entry (GSE) to optimize the coal pillar width and support measures. We draw the following conclusions:

- The monitored roadway deformation indicates that the maximum roof-to-floor and rib-to-rib convergence in the first 1000 m of the roadway reached 860 mm and

1460 mm, respectively. As shown in the photographs taken by a borehole camera, the 7-m coal pillar yielded completely to the coalescence of internal cracks.

- A UDEC Trigon model was developed to simulate roadway deformation and crack distribution in the yield pillar. The input parameters were calibrated, and the global model was validated against data from field monitoring. The simulated results are consistent with those from field observations. The initiation, propagation, and coalescence of internal cracks were investigated throughout the formation process of the coal pillar, including the 15108 longwall mining and 15106 tailgate excavation processes. Shear cracks played a predominant role in the pillar failure, which propagated from the pillar surface to its center. Under the conditions of the 15106 tailgate, the most appropriate coal pillar width was determined to be 10 m.
- According to the coal pillar damage analysis, an optimal pillar width and support measures were proposed and implemented in the last 600 m of 15106 tailgate. Field applications show that the resulting roof-to-floor and rib-to-rib convergence are 216 mm and 285 mm, respectively, representing a reduction of approximately 80%. These support recommendations provide a basis for controlling the deformation of gob-side yield pillars under similar engineering and geological conditions.

Acknowledgements This research has been supported by the Fundamental Research Funds for the Central Universities (2017XKZD06). The authors thank Sijiazhuang coal mine for their support during the field test. Also, this article benefited from valuable comments and suggestions by co-editors and other anonymous reviewers.

References

- Bai JB, Shen WL, Guo GL, Yu Y (2015) Roof deformation, failure characteristics, and preventive techniques of gob-side entry driving heading adjacent to the advancing working face. *Rock Mech Rock Eng* 48(6):2447–2458. <https://doi.org/10.1007/s00603-015-0713-2>
- Carr F, Martin E, Gardner BH (1985) How to eliminate roof and floor failures with yield pillar. *Coal Min Part II* 21:44–49
- Coulthard MA (1999) Applications of numerical modelling in underground mining and construction. *Geotech Geol Eng* 17:373–385. <https://doi.org/10.1023/A:1008951216602>
- De Borst R, Sluys LJ, Mühlhaus HB, Pamin J (1993) Fundamental issues in finite element analysis of localization of deformation. *Eng Comput* 10(2):99–122. <https://doi.org/10.1108/eb023897>
- Elmo D (2006) Evaluation of a hybrid FEM/DEM approach for determination of rock mass strength using a combination of discontinuity mapping and fracture mechanics modelling, with particular emphasis on modelling of jointed pillars. Ph.D. thesis. Camborne School of Mines, University of Exeter
- Elmo D, Stead D (2010) An integrated numerical modelling–discrete fracture network approach applied to the characterisation of rock mass strength of naturally fractured pillars. *Rock Mech Rock Eng* 43(1):3–19. <https://doi.org/10.1007/s00603-009-0027-3>
- Gao FQ (2013) Simulation of failure mechanisms around underground coal mine openings using discrete element modelling. PhD thesis. Simon Fraser University, Burnaby
- Gao W, Ge M (2016) Stability of a coal pillar for strip mining based on an elastic–plastic analysis. *Int J Rock Mech Min Sci* 87:23–28. <https://doi.org/10.1016/j.ijrmms.2016.05.009>
- Gao FQ, Kang HP (2016) Effects of pre-existing discontinuities on the residual strength of rock mass—insight from a discrete element method simulation. *J Struct Geol* 85:40–50. <https://doi.org/10.1016/j.jsg.2016.02.010>
- Gao FQ, Stead D (2014) The application of a modified Voronoi logic to brittle fracture modelling at the laboratory and field scale. *Int J Rock Mech Min Sci* 68(68):1–14. <https://doi.org/10.1016/j.ijrmms.2014.02.003>
- Gao FQ, Stead D, Kang HP (2015) Numerical simulation of squeezing failure in a coal mine roadway due to mining-induced stresses. *Rock Mech Rock Eng* 48(4):1635–1645. <https://doi.org/10.1007/s00603-014-0653-2>
- Hill D (2005) Coal pillar design criteria for surface protection. In: Proceedings of the coal 2005 conference, 26–28 April 2005
- Hoek E, Brown ET (1997) Practical estimates of rock mass strength. *Int J Rock Mech Min Sci* 34(8):1165–1186. [https://doi.org/10.1016/S1365-1609\(97\)80069-X](https://doi.org/10.1016/S1365-1609(97)80069-X)
- Itasca Consulting Group Inc (2014) UDEC (universal distinct element code), version 6.0. Itasca, Minneapolis
- Jaiswal A, Shrivastva BK (2009) Numerical simulation of coal pillar strength. *Int J Rock Mech Min Sci* 46(4):779–788. <https://doi.org/10.1016/j.ijrmms.2008.11.003>
- Kang HP, Lin J, Yan LX, Zhang X, Wu YZ (2009) Study on characteristics of underground in-situ distribution in Shanxi coal mining fields. *Chin J Geophys* 52(7):1782–1792
- Kazerani T, Zhao J (2010) Micromechanical parameters in bonded particle method for modelling of brittle material failure. *Int J Numer Anal Methods Geomech* 34(18):1877–1895. <https://doi.org/10.1002/nag.884>
- Li WF, Bai JB, Peng SS, Wang XY, Xu Y (2015) Numerical modeling for yield pillar design: a case study. *Rock Mech Rock Eng* 48(1):305–318. <https://doi.org/10.1007/s00603-013-0539-8>
- Lisjak A, Grasselli G (2014) A review of discrete modeling techniques for fracturing processes in discontinuous rock masses. *J Rock Mech Geotech Eng* 6(4):301–314. <https://doi.org/10.1016/j.jrmge.2013.12.007>
- Lorig LJ, Cundall PA (1989) Modeling of reinforced concrete using the distinct element method. In: Fracture of concrete and rock. Springer, New York, pp 276–287
- Maleki H (1992) In situ pillar strength and failure mechanisms for US coal seams. In: Proceedings of the workshop on coal pillar mechanics and design. US States Bureau of Mines, Pittsburgh, IC-9315, pp 73–78
- Mayer JM, Stead D (2017) Exploration into the causes of uncertainty in UDEC grain boundary models. *Comput Geotech* 82:110–123. <https://doi.org/10.1016/j.compgeo.2016.10.003>
- Mortazavi A, Hassani FP, Shabani M (2009) A numerical investigation of rock pillar failure mechanism in underground openings. *Comput Geotech* 36(5):691–697. <https://doi.org/10.1016/j.compgeo.2008.11.004>
- Peng SS (2006) Longwall mining, 2nd edn. Peng SS Publisher, Morgantown
- Pine RJ, Coggan JS, Flynn ZN, Elmo D (2006) The development of a new numerical modelling approach for naturally fractured rock masses. *Rock Mech Rock Eng* 39(5):395–419. <https://doi.org/10.1007/s00603-006-0083-X>

- Poulsen BA (2010) Coal pillar load calculation by pressure arch theory and near field extraction ratio. *Int J Rock Mech Min Sci* 47(7):1158–1165. <https://doi.org/10.1016/j.ijrmms.2010.06.011>
- Salamon MDG (1970) Stability, instability and design of pillar workings. *Int J Rock Mech Min Sci Geomech* 7(6):613–631. [https://doi.org/10.1016/0148-9062\(70\)90022-7](https://doi.org/10.1016/0148-9062(70)90022-7)
- Salamon MDG, Munro AH (1967) A Study of the strength of coal pillars. *J S Afr Inst Metall* 68:55–67
- Singh M, Seshagiri Rao K (2005) Empirical methods to estimate the strength of jointed rock masses. *Eng Geol* 77:127–137. <https://doi.org/10.1016/j.enggeo.2004.09.001>
- Wang SL, Hao SP, Chen Y, Bai JB, Wang XY, Xu Y (2016a) Numerical investigation of coal pillar failure under simultaneous static and dynamic loading. *Int J Rock Mech Min Sci* 84:59–68. <https://doi.org/10.1016/j.ijrmms.2016.01.017>
- Wang WJ, Yuan C, Yu WJ, Wu H, Peng WQ, Peng G, Liu XS, Dong EY (2016b) Stability control method of surrounding rock in deep roadway with large deformation. *J China Coal Soc* 41(12):2921–2931 2016. 1115
- Yu B, Zhang ZY, Kuang TJ, Liu JR (2016) Stress changes and deformation monitoring of longwall coal pillars located in weak ground. *Rock Mech Rock Eng* 49(8):3293–3305. <https://doi.org/10.1007/s00603-016-0970-8>
- Zhang L, Einstein HH (2004) Using RQD to estimate the deformation modulus of rock masses. *Int J Rock Mech Min Sci* 41(2):337–341. [https://doi.org/10.1016/S1365-1609\(03\)00100-X](https://doi.org/10.1016/S1365-1609(03)00100-X)
- Zhang GC, He FL, Jia HG, Lai YH (2017) Analysis of gateroad stability in relation to yield pillar size: a case study. *Rock Mech Rock Eng* 50:1263–1278. <https://doi.org/10.1007/s00603-016-1155-1>

Publisher's Note Springer Nature remains neutral with regard to jurisdictional claims in published maps and institutional affiliations.